RECENT CRUSTAL MOVEMENTS ALONG THE CARMEL FAULT SYSTEM, ISRAEL

R.N. Nof [1,2], G. Baer [2], Y. Eyal [1], F. Novali [3]

[1] Department of Geological and Environmental Sciences, Ben-Gurion University of the Negev, P.O. Box 653, Beèr-Sheva 84105, Israel, Email: novitsky@bgu.ac.il
[2] Geological Survey of Israel, 30 Malkhe Yisrael St., Jerusalem 9550, Israel, Email: baer@gsi.gov.il
[3] Tele-Rilevamento Europa - TRE, Via Vittoria Colonna 7, Milano, 20149 Italy, Email: fabrizio.novali@treuropa.com

ABSTRACT

A long-standing dilemma in the geology of Israel is whether the Carmel Fault (CF) is currently active and to what extent does it contribute to the seismic hazard of the city of Haifa and the nearby petrochemical industrial area. In this study we use InSAR stacking and PSInSAR to measure the surface movements on both sides of the CF. Processing single interferograms showed low signal to noise ratio (SNR), and no consistent sense of apparent displacements. Stacking interferograms improved the SNR, but uncertainties still remained high, compared to the signal. PSInSAR analysis shows no evidence for differential surface movements between the two sides of the CF. Using elastic dislocation modeling we find that the lower detection limits on the NW-SE segments of the fault, are 1 mm/year for vertical movement and 4 mm/year for horizontal sinistral movement. Thus, we cannot exclude creep along the Carmel Fault at rates lower than these limits.

1. INTRODUCTION

The Carmel Fault (CF) is the northern part of the Carmel-Fari'a Fault System (CFFS) that splays off the Dead Sea Fault (DSF) and continues northwestwards into the Mediterranean Sea [1, 2, 3, 4, 5]. The CF is composed of a short central N-S striking segment between southern and northern NW-SE striking segments (Fig 1). The surface exposure of the CFFS is not continuous along its course [1, 6]. The northwestern segment of the fault crosses the city of Haifa and its suburbs and passes a few km away from the petrochemical industry in the Haifa Bay. Based on geological, geophysical and geomorphological data the CF has been considered to be potentially active along the majority of its course [7]. Yet, defining the CF as active is not unequivocal. The earthquake catalogue (GII, 2006) and a recent earthquake relocation study [8] show a lack of seismic energy production along the northern fault segments during the last 20 years. The largest earthquake in northern Israel, outside the DSF, during the past 50 years, with a magnitude of M_L = 5.3, occurred on August 24, 1984 about 8 km east of the central segment of the CF (Fig 1). Paleoseismic studies [9, 10] did not detect any fault activity younger than a few 10000s years or evidence for liquefaction in the Holocene sediments of the Haifa Bay [11]. Recently, a seismic profile across the northern segment of the CF has failed to reveal any disturbance in late Pleistocene sediments overlying the fault trace [12]. Thus, there is a growing need for precise mapping and reliable data of the Carmel fault segments to determine a possible Recent activity along the CF. The CF is characterized by both dip-slip and strike-slip components, however, the sense of recent motion is still ambiguous. In contrast with a suggested sinistral displacement which was based

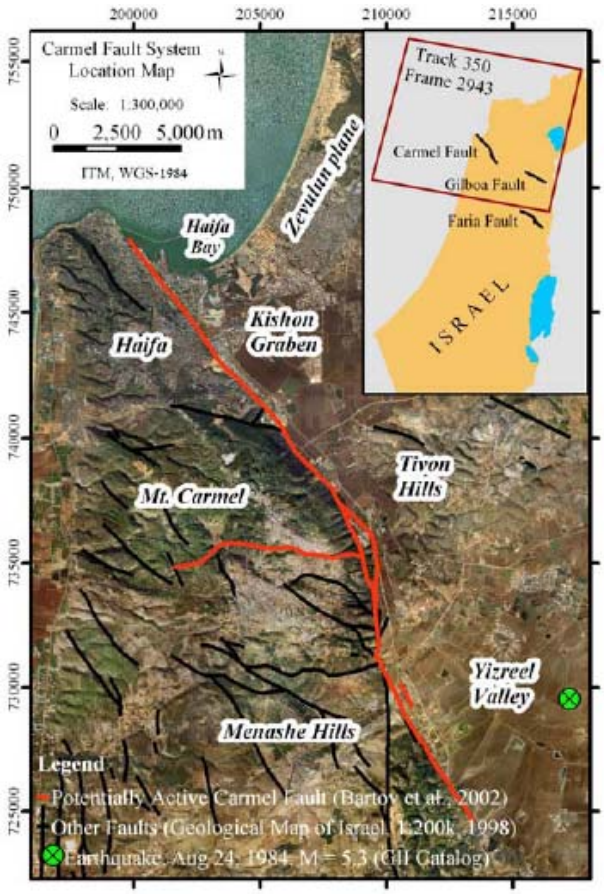

Figure 1 - Location Map of the research area and satellite Image coverage of frame 2943 track 350 (insert), superimposed on an orhtorectified aerial photograph (orthophoto). The red line marks the Carmel fault described as a potentially active fault [7]. Black lines are tracks of surface mapped faults (From GSI GIS database). The green circle shows the location of the August 24, 1984 M=5.3 earthquake (GII earthquake catalog).

on geomorphologic and tectonic considerations [9, 13, 14], a recent GPS study suggests dextral displacement [15]. Focal plane solutions of the larger earthquakes show sinistral components along SE–NW faults, in agreement with the geological and geomorphologic observations.

In this study we use InSAR stacking and PSInSAR to find evidence for possible differential movements between both sides of the CF which may indicate recent activity. We also use elastic modeling to constrain the detection limits of the technique and evaluate the possible deformation mechanisms.

2. PREVIOUS STUDIES

Previous estimates of the slip rate along the CF relied on displacements of dated markers, such as sedimentary units or stream channels, and geodetic measurements. As summarized by [13], most studies show sinistral displacement along the CF. A vertical displacement of 2 cm per 1000 years (0.02 mm/y) along the N-S segment of the CF was suggested by [14], based on seismic profiles. A vertical displacement rate of 0.2 mm/y was estimated from displaced 55,000 y old layers which were found in shallow seismic profiles on the NW segment of the CF [16]. A left-lateral displacement of 500–1500 m during the Pleistocene was suggested from geomorphologic evidences [13], implying a horizontal slip rate of less than 1 mm/y. Recent GPS and precise leveling measurements reveal a relative uplift of Mt. Carmel (or subsidence of the surrounding areas) at a rate of 5 mm/y during the years 1990 to 1999 [17]. Later leveling results show that compared to the Carmel slopes, the deformation of the center of Mt. Carmel can be divided into a period of uplift (1987 to 1992) and a period of subsidence (1992 to 2003) [18]. As for the horizontal component, the GPS results are also somewhat controversial, ranging from 3.5 mm/y dextral slip [15], through 0.9±1.1 mm/y sinistral slip [19] to about 4 mm/y sinistral slip [18].

3. METHODS

We present here the first use in Israel of stacking and Permanent Scatterers (PS) InSAR. The basic assumption of the two techniques is that the deformation rate along a fault is constant during the analyzed period while atmospheric errors or other noise (e.g. thermal) are random. The stacking method enables to minimize the random noise [20]. Our stacking procedure follows in part that of [21]. We first create chains of interferograms with short baselines (see below) along the analyzed time period. Then we sum the phase changes from all the available interferometric pairs in each chain, and divide the sum by the total time span of the measurements. By using interferometric chains, almost all images are used both as "slaves" and as "masters", thus eliminating the atmospheric signals embedded in each image and minimizing the atmospheric errors to those of the first and last images in the chain. Averaging N chains will reduce the atmospheric signal by $\sqrt{N}$. In fact, this procedure creates fewer interferograms with longer temporal baselines which contain potentially higher deformation signal than the short time span interferograms. In the case of this research it also enabled us to use more images than with a stacking attitude which uses only independent interferograms (e.g. [21]). Finally, in chains where the deformation rates of more than 5% of the pixels in the Mt. Carmel area are greater than 2σ of the total stack, we removed the first or last interferogram of the chain. We repeat this process until no chain has more than 5% pixels in the Carmel region with deformation rates greater than 2σ of the total stack.

Permanent Scattering Interferometric Synthetic Aperture Radar (PSInSAR) enables estimation and removal of atmospheric effects by combining and analyzing data from long time series of SAR images [22, 23]. Relative target LOS velocity can then be estimated with accuracy, often better than 1 mm/yr, due to the long time span, depending, among other factors, on the number of scenes and the atmospheric conditions during the different SAR acquisitions. For some of the points a time series of their estimated motion can also be made. The results are computed with respect to a ground control point (GCP) of known elevation and are relative to its motion. Data for this study includes 53 SAR images from the European Space Agency's ERS-1 and ERS-2 satellites of descending track 350, frame 2943 (Fig 1) acquired during the years 1992-2001. For the stacking method the data was processed using the ROI-PAC software [24], at an 8-looks resolution (~160X160 m/pixel). This resolution increases the detectable signal coverage but reduces the sensitivity to small-scale features. In order to increase the SNR, a filter that takes into account the coherence value of the pixel was used. Following the study of [25], double filtering was performed enabling to increase the available area for analysis. Of the available 53 raw images, 45 were processed to SLC (single look complex) images. Out of 105 possible pairs with low baselines, 27 pairs with an average baseline of 38 m (and a maximum of 102 m) were selected according to the signal coverage area (Fig 2). The topographic signal was removed using the 50m resolution Survey of Israel DEM combined with the 25m Israel DEM [26], and the 3 arc sec (~90 m) SRTM DEM [27]. We used satellite orbits provided by Delft Institute for Earth-Oriented Space research (DEOS), The Netherlands [28]. The PSInSAR Processing was carried out by T.R.E Milan within the framework of the Terrafirma Pan-European service for ground motion hazards under the European Space Agency GMES (Global Monitoring for Environment and Security) project. All interferograms used one Master scene from September 26, 1997. The data consist of 35,000 permanent scatterers (PS) that

were measured for their average velocity, of which 16,000 were also analyzed for their time-series behavior.

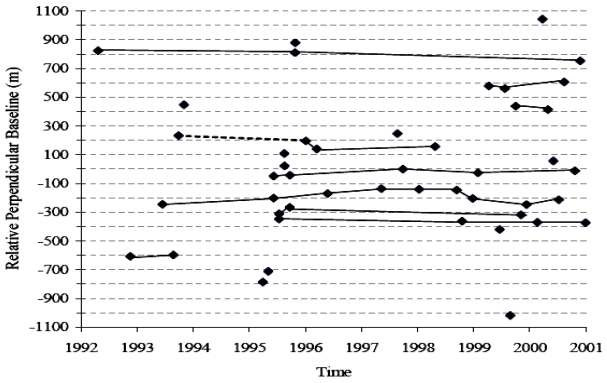

Figure 2 - Frame 2943 track 350 acquisitions dates and perpendicular baselines. Baselines are calculated with respect to the September 26, 1997 Image. Solid lines represent pairs of interferograms used for this research. Dashed line represents an interferometric pair which failed to spatially synchronize and therefore was not included in the calculations.

4. RESULTS

4.1. Stacking

Individual interferograms show strong effects of atmospheric stratification and turbulence. Opposite LOS range changes appear in different interferograms that span the same time interval, and in places, the apparent deformation rate is unrealistically high (Fig 3). In some cases, two interferograms that have a common image, one as a master and the other as a slave, show opposite phase changes with a similar spatial pattern. Of the 27 low-baseline interferograms, 6 interferograms were eliminated from the stacking analysis due to their poor coherence.

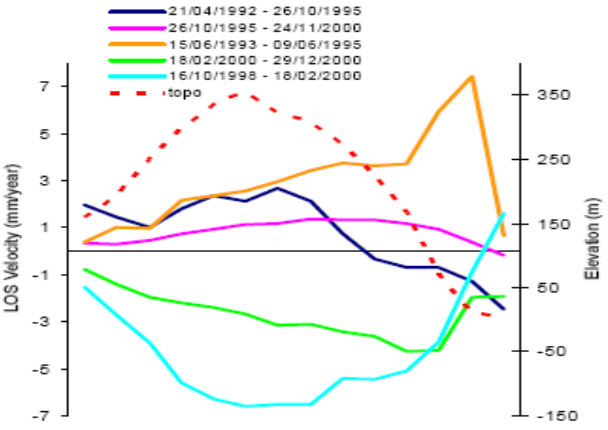

Figure 3 – Topography and Average LOS annual velocity (mm/year) of 5 representive interferograms along profile A-A` shown in Fig 4. Note that interferograms with similar time coverage show different and in places opposite LOS change.

The remaining 21 interferograms were arranged in chains with low (<100 m) perpendicular baselines and a cumulative time span of about 30 years. The apparent deformation rates are between 12 and -12 mm/y with a standard deviation of ±30 mm/y. These values are unreasonably high for surface deformation and probably result from atmospheric signals at the end members of each interferometric chain. By eliminating 5 end interferograms from chains that show high standard deviations, significant improvement is made. The new stack is composed of 6 chains having a cumulative time span of about 27 years and the apparent deformation rate has been reduced to values between 3 and -3 mm/y with standard deviations of ±6 mm/y (Fig 4). This improvement is demonstrated in the cross section A-A', that shows average deformation rates, standard deviations, and topography, sampled in 10X10 pixel bins (~500X500 m) along the profile (Fig. 5 a & b). The high standard deviation values that still remain after this procedure suggest that the apparent deformation rates are statistically insignificant and no tectonic implication can thus be drawn from these results.

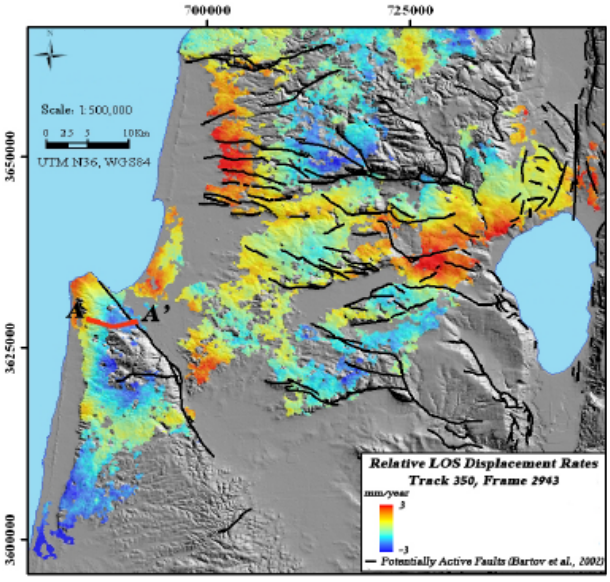

Figure 4 - Stacking results of 16 interferograms with a total time span of about 27 years. Profile A-A' (in red) is shown in Fig 5.

4.2. PSInSAR

The major part of Mt. Carmel is a national forest with a relatively small number of permanent scatterers. Most of the scatterers in the region are buildings in the city of Haifa and its suburbs. Fig 6 shows the PSInSAR average annual velocity map. In the northern part of the Carmel Mountain, where the city of Haifa is located, there is no distinct deformation pattern. A profile across the northern part of the Carmel Fault (Fig 5c) shows rates in the range of +0.1 to -0.6 mm/y, with no significant variation across the fault. The estimated standard deviations are smaller than ±0.3 mm/y. The

map shows local subsidence with rates up to 7 mm/y in the area of the Zevulun plane, particularly near the outlet of the Kishon River. These observations were confirmed in the field by the occurrence of cracked buildings and deformed pavements.

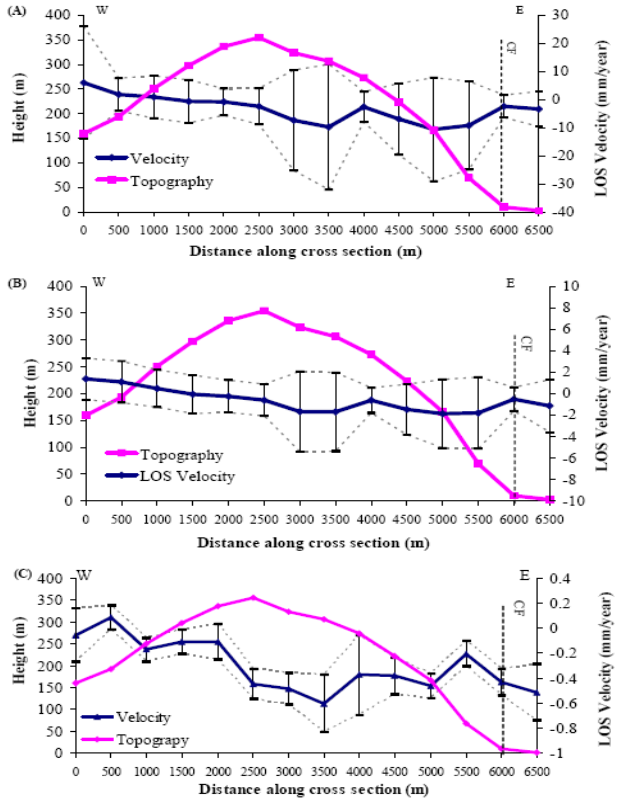

Figure 5 - Profile A - A'. (A) Of all available stacked interferograms; (B) After removing data with high deviation (Fig 4); (C) PSInSAR results (Fig 6); Note that the LOS velocity scale of each profile is different. Vertical black Dashed line show the location of the Carmel Fault (CF). Grey thin dashed lines show the standard deviation limits. Each point along the profile is an average of a 10X10 pixel bin (500X500 m).

5. DISCUSSION

Our PSInSAR results show no evidence for differential surface displacement across the Carmel Fault in the satellite to ground LOS. This does not necessarily rule out the possibility that slip occurs at a rate, depth, or rake that is undetectable in the satellite geometry and resolution. To examine the detection limits of displacements we use elastic dislocation models [29, 30] which calculate the expected surface deformation with respect to the satellite for different fault parameters (location, strike, dip, rake, slip, and dimensions) in a homogenous medium. Since there are very few permanent scatterers to compare with along the N-S segment of the CF, the models are constructed only for the NW-SE segment. The fault dip was set to 60° to the NE, based on the focal plane solution of the 1984 M_L=5.3 earthquake [31]. The width of the fault was set to the depth of the continental crust, estimated to be 35 km in this area [32]. In order to avoid effects of the fault tips, the length of the fault was set to infinity by extending its limits beyond the research area.

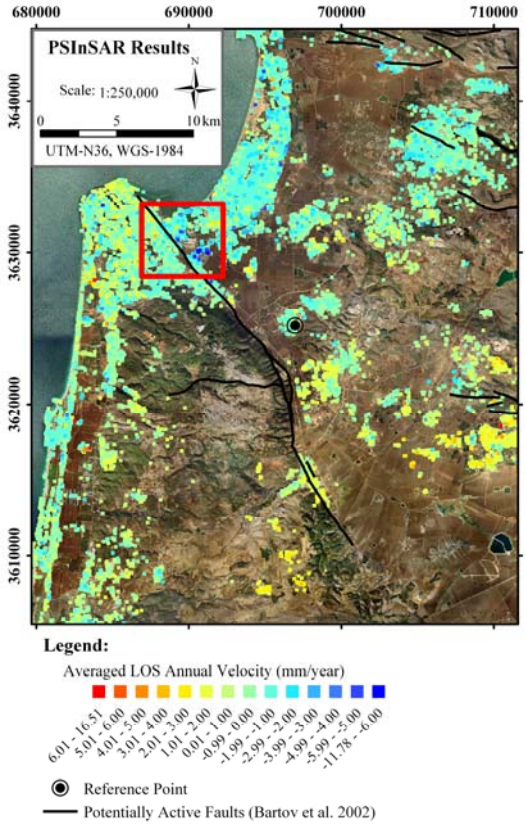

Figure 6 - PSInSAR Results. PS Averaged annual LOS velocity, superimposed over an orthorectified aerial photo (Orthophoto). Red colors indicate movement toward the satellite (e.g. uplift), blue colors indicate movement away from the satellite (e.g. subsidence); The red square area shows the location of high subsidence confirmed in the field.

We constructed models for the NW-SE and N-S segments, in which the depth from the surface to the top of the fault, the rake, and the slip rate were iteratively changed. The maximum slip rate in our models is 5 mm/yr, corresponding to the GPS estimates [15]. We checked rakes of 0° (left-lateral displacement), 90° (normal), -90° (reverse), and 40° (oblique). Surface rupture is represented by setting the depth to the top of the fault to zero. Fig 7 shows synthetic interferograms of the predicted LOS displacements in our models.

As previously noted, the PSInSAR technique is limited to detect LOS deformation higher than 1 mm/y. Thus, because no displacement was observed along the CF, fault model parameters which yield rates that are less than 1 mm/yr at surface cannot be excluded. Fig 8 shows all the combinations of slip, rake, and depth to

the top of the fault rupture, where the LOS displacement does not exceed 1 mm/yr. These values place upper constraints on the possible displacement along the fault. In the NW-SE segment the PSInSAR method has a dip-slip rate detection limit of 1 mm/y. Higher slip rates would create higher LOS deformations and would be detected. Left lateral slip along this segment is limited to 4 mm/y at a 1 km upper locking depth of the fault.

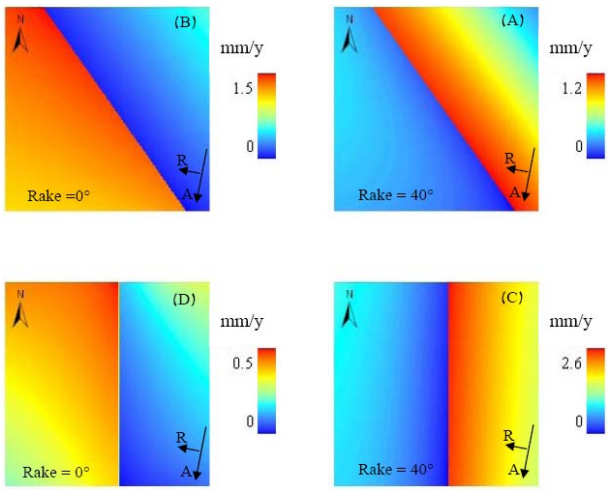

Figure 7 - Four representative Synthetic interferograms showing the expected surface LOS velocity change. The models were defined by a slip rate of 5 mm/y; depth to bottom of fault – 35 km, top of the fault was set at surface; dip - 60° east; the arrows show the satellite azimuth – A and range – R; red colors represent relative displacements toward the satellite and blue colors represent relative displacements away from satellite; (A) Strike 325° and rake 40°; (B) Strike 325° and rake 0°; (C) Strike 0° and rake 40°; (D) Strike 0° and rake 0°.

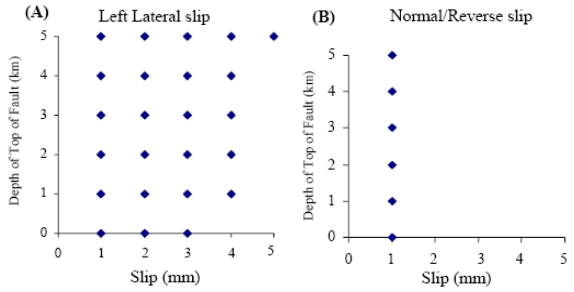

Figure 8 - Possible combinations (marked as blue rhombs) of slip Rates and depth to top of fault that may occur but can not be detected by PSInSAR for a 325° striking fault. (A) Left lateral slip. (B) Normal or reverse slip.

6. CONCLUSIONS

The interferograms used in this study are characterized by a low signal to noise ratio. Although we used different signal enhancing methods and approaches we could not find any evidence for differential surface displacement along the Carmel Fault. The PSInSAR showed high sensitivity to local effects. Subsiding areas found in the Haifa Bay resulted most likely from compaction of clay-rich layers, and possibly in response to groundwater level drop.

The stacking and PSInSAR techniques assume a uniform slip rate with time. Despite the fact that no surface displacement was found, the models show that a vertical slip of up to 1 mm/y, or horizontal slip of up to 4 mm/y along the NW-SE segments of the CF, although unlikely, cannot be totally rejected. These estimations are higher than those found by the geological observations [13, 14, 16]. The long recurrence intervals of M>6 earthquakes along the CF may also suggest that some of the accumulating strain along the fault might be released continuously by aseismic creep or by small earthquakes.

7. ACKNOWLEDGMENTS

This research was funded by the ministerial committee on earthquake preparedness. ERS data were provided by the European Space Agency (ESA) under category 1 project 1058. We are grateful to Tim Wright, Gareth Funning, and Barry Parsons of COMET, University of Oxford, UK, for their help and hospitality.

8. REFERENCES

1. Picard, L. & Kashai, E. (1958). On the Lithostratigraphy and Tectonics of the Carmel. *Bull. Res. Counc. Israel*. **7G**(1), 1–19.
2. Arad, A. (1965). Geological outline of the Ramot-Menashe region (northern Israel) *Isr. J. Earth Sci*. **14**, 18-32.
3. Freund, R. (1965). A Model of Structural Development of Israel and Adjacent Areas since the Upper Cretaceous times. *Geol. Mag.* **102**, 189-205.
4. Ben-Avraham, Z. & Hall, J.K. (1977). Geophysical Survey of Mount Carmel Structure and its extension into the eastern Mediterranean. *J. Geophys. Res*. **82**, 793-802.
5. Garfunkel, Z., Zak I. & Freund, R. (1981). Active faulting in the Dead Sea Rift. *Tectonophysics*. **80**, 81-108.
6. Rotstein, Y., Shaliv G. & Rybakov, M. (2003). Active tectonics of the Yizre'el Valley, Israel, using high-resolution seismic reflection data. *Tectonophysics*. **382**, 31-50.
7. Bartov, Y., Sneh, A., Fleischer, L., Arad V. & Rosensaft, M. (2002). Potentially active faults in Israel. *Geological Survey of Israel Report GSI/29/2002*. pp8.
8. Shamir, G. (2007). *Personal Communication*.
9. Gluck, D. (2002). The landscape evolution of the southwestern Dead Sea basin and the paleoseismic record of the southwestern marginal fault of the Dead Sea basin and of

the Carmel fault during the late Pleistocene and Holocene. *Geological Survey of Israel Report GSI/4/02*. pp86 (in Hebrew, with English abstract).

10. Zilberman, E. (2007). *Pers. Communication.*
11. Heimann, A., Frydman, S., Wachs, D. & Talwani, P. (2001). Seismic hazard evaluation of Haifa and Eilat bay areas, Israel. *Geological Survey of Israel, Report GSI/40/2001*. pp109.
12. Medvedev, B., Ben-Gai, Y., Frieslander U. & Bartov, Y. (2006). Carmel Fault age-constraint, new evidence from high resolution geophysical study. *Abs. IGS Ann. Meeting*, Bet-Shean, Israel, pp86.
13. Achmon, M. (1986). The Carmel border fault between Yoqneam and Nesher. *M.Sc thesis*, Hebrew University of Jerusalem, Jerusalem. pp56. (in Hebrew, with English abstract).
14. Rotstein, Y., Bruner I. & Kafri, U. (1993). High-resolution seismic imaging of the Carmel Fault and its implications for the structure of Mt. Carmel. *Isr. J. Earth Sci*. **42**, 55-69.
15. Agmon, E. (2001). Algorithm for the analysis of deformation monitoring networks. *M.Sc. Thesis*, Technion, Israel Institute of Technology, Haifa. pp117 (in Hebrew, with English abstract).
16. Salamon, A., Zaslavsky, Y., Shtivelman, V. & Rockwell, T. (2001). Seismic hazards analysis in the Nesher site: Bay of Haifa, Israel. Abs. *IGS, Ann. Meeting march 2001*. 85 and 101.
17. Even Tzur, G. & Agmon, E. (2005). Monitoring vertical movements in Mt. Carmel by means of GPS and precise leveling, *Survey Rev*. **38**(596), 146-157.
18. Shahar, L. & Even Tzur, G. (2005). Recent vertical movements inferred from high-precision leveling data in the Carmel Mountain. *Isr. J. Earth Sci*. **54**, 219-228.
19. Ostrovsky, E. (2005). The G1 geodetic-geodynamic network: results of the G1 GPS surveying campaigns in 1996/1997 and 2001/2002. *Tech. Proj. Rep*., Survey of Israel. pp50.
20. Zebker, H.A., Rosen P. & Hensley, S. (1997). Atmospheric artifacts in interferometric synthetic aperture radar surface deformation and topographic maps, *J. Geophys. Res*. **102**, 7547-7563.
21. Schmidt, D.A., Bürgmann, R., Nadeau R.M. & d'Alessio, M. (2005). Distribution of aseismic slip rate on the Hayward Fault inferred from seismic and geodetic data. *J. Geophys. Res*. **110**(B8), Art. No. B08406.
22. Ferreti, A., Prati, C. & Rocca, F. (2001). Permanent Scatterers in SAR interferometry. *IEEE Trans. Geosci. Remote Sense*. **39**(1), 8-20.
23. Colesanti, C., Ferretti, A., Prati C. & Rocca, F. (2003). Monitoring landslides and tectonic motions with the Permanent Scatterers technique. *Engineering Geology*. **68**, 3-14.
24. Rosen, P.A., Henseley, S., Peltzer, G. & Simons, M. (2004). Updated Repeat Orbit Interferometry Package Released. *EOS Trans. AGU*, **85**(5), 35.
25. Holley R. (2004). Interseismic deformation on the North Anatolian Fault from Interferometric Synthetic Aperture Radar. *MSc. Thesis*, University of Oxford, Oxford. pp66.
26. Hall, J.K. (1993). The GSI Digital Terrain Model (DTM) project completed. *Israel Geological Survey Current Research*. **8**, 47–60.
27. Farr, T.G. & Kobrick, M. (2000). Shuttle Radar Topography Mission produces a wealth of data. *Amer. Geophys. Union Eos*. **81**, 583-585.
28. Scharro, R. & Visser, P. (1998). Precise orbit determination and gravity field improvement for the ERS satellites. *J. Geophys Res*. **103**, 8113-8127.
29. Okada Y. (1985). Surface deformation due to shear and tensile faults in a half-space. *Bull. seism. Soc. Am*. **135**, 1135–1154.
30. Okada Y. (1992). Internal deformation due to shear and tensile faults in a half-space. *Bull. seism. Soc. Am*. **82**, 1018–1040.
31. Hofstetter, A., van Eck T. & Shapira, A. (1996). Seismic activity along fault branches of the Dead Sea-Jordan Transform System: The Carmel-Tirza Fault System. *Tectonophysics*, **267**, 317-330.
32. Ginzburg, A., Ben-Avraham, Z., Makris, J., Hubral P. & Rotstein, Y. (1994). Crustal structure of northern Israel. *Mar. Petrol. Geol*. **11**, 501-506.